

68.9% Efficient GaAs-Based Photonic Power Conversion Enabled by Photon Recycling and Optical Resonance

Henning Helmers,* Esther Lopez, Oliver Höhn, David Lackner, Jonas Schön, Meike Schauerte, Michael Schachtner, Frank Dimroth, and Andreas W. Bett

For solar cells operating under the broad-band solar spectrum, the photovoltaic conversion efficiency is fundamentally limited by transmission and thermalization losses. For monochromatic light, these losses can be minimized by matching the photon energy and the absorber material's bandgap energy. Furthermore, for high-crystal-quality direct semiconductors, radiative recombination dominates the minority carrier recombination. Light-trapping schemes can leverage reabsorption of thereby internally generated photons. Such photon recycling increases the effective excess carrier concentration, which, in turn, increases photovoltage and consequently conversion efficiency. Herein, a back surface reflector underneath a GaAs/AlGaAs rear-heterojunction structure leverages photon recycling to effectively reduce radiative recombination losses and therefore boost the photovoltage. At the same time, resonance in the created optical cavity is tailored to enhance near-bandgap absorption and, thus, minimize thermalization loss. With a thin film process and a combined dielectric–metal reflector, an unprecedented photovoltaic conversion efficiency of $68.9 \pm 2.8\%$ under 858 nm monochromatic light at an irradiance of 11.4 W cm^{-2} is demonstrated.

avoidance of electromagnetic interference, lightning protection, explosion protection, compatibility with strong electromagnetic fields, and the possibility of free-space power beaming. Another key advantage is the prospect of a purely optical power and data transmission link when combined with optical communication.^[1–5] The application space for this technology includes sensors in special environments (structural health monitoring of wind turbines,^[6] monitoring of high-voltage transmission lines^[7–10]), wireless powering of medical implants,^[11–15] optically isolated power supply for electronic systems,^[16–18] optical powering of remote antenna units,^[2,19–21] optically powered networks,^[22,23] Internet-of-Things devices,^[24] and optical wireless power transfer.^[25–29]

Several groups have demonstrated PPCs based on III–V compound semiconductor materials with remarkable power conversion efficiencies well above 50%.^[30–50]

To maximize performance, the tradeoff


between transmission and thermalization losses needs to be balanced. As an example, when a $3 \mu\text{m}$ thick GaAs absorber (bandgap energy $E_g = 1.424 \text{ eV}$) is illuminated with 830 nm laser light (photon energy $E_{ph} = 1.494 \text{ eV}$), 4.7% of the laser power is lost by thermalization to the crystal lattice, whereas about 4.2% is transmitted and lost due to limited absorptance. While increasing absorber thickness shifts the optimum of this tradeoff toward the bandgap,^[39] insufficient minority carrier diffusion length in the absorber counteracts this gain.

In this work, we alter the boundary conditions of this optimization problem; namely we introduce a back surface reflector (BSR) beneath the active photovoltaic layers to trap photons in the resulting optical cavity. On one hand, thereby we exploit Fabry–Perot resonances in the cavity^[51,52] to increase spectral absorptance for otherwise weakly absorbed near-bandgap photon energies. In turn, we maximize spectral response (SR) close to the bandgap and, thus, simultaneously minimize both transmission and thermalization losses. On the other hand, the optical cavity impacts the luminescence behavior of the device. Photons generated internally by radiative recombination are trapped inside the cavity. Given the back reflector, their only escape route is the front side, where total internal reflection at the semiconductor/air interface restricts the escape cone to approximately 16° which yields 95.6% reflectance (assuming

1. Introduction

In recent years, photonic power converters (PPCs), also known as photovoltaic cells for monochromatic light, laser power converters, or sometimes phototransducers, have received increasing interest as they enable a growing number of optically powered applications. Wireless or fiber-based optical power transmission offers unique advantages such as inherent galvanic isolation,

Dr. H. Helmers, Dr. E. Lopez, Dr. O. Höhn, Dr. D. Lackner, Dr. J. Schön, M. Schauerte, M. Schachtner, Dr. F. Dimroth, Prof. A. W. Bett
Fraunhofer ISE
Fraunhofer Institute for Solar Energy Systems
Heidenhofstr. 2, 79110 Freiburg, Germany
E-mail: henning.helmerts@ise.fraunhofer.de

 The ORCID identification number(s) for the author(s) of this article can be found under <https://doi.org/10.1002/pssr.202100113>.

© 2021 The Authors. physica status solidi (RRL) Rapid Research Letters published by Wiley-VCH GmbH. This is an open access article under the terms of the Creative Commons Attribution-NonCommercial License, which permits use, distribution and reproduction in any medium, provided the original work is properly cited and is not used for commercial purposes.

DOI: 10.1002/pssr.202100113

isotropic internal emission). Consequently, despite weak absorption at the bandgap these photons are eventually mostly reabsorbed. This effect, known as photon recycling,^[53–56] is relevant for direct semiconductors of sufficient material quality, i.e., where nonradiative recombination is small enough. It can be equivalently regarded as an effective decrease in radiative recombination, a prolongation of the effective carrier lifetime, and an increase in internal photon density, which ultimately leads to a boost in voltage. Overall, we exploit optical resonance and photon recycling to benefit in current and voltage, respectively.

2. Results

We have fabricated thin-film PPCs (designated area $A = 0.054 \text{ cm}^2$) with different back reflectors (Figure 1h). A n-GaAs/p-AlGaAs rear-heterojunction (see Figure 1a and Section 4 for details of the epitaxial structure) approach is pursued to effectively suppress recombination in the space charge region.^[57,58] Apart from a reference sample on GaAs substrate, we analyze two different back reflectors: one is formed by direct gold deposition, the other by a combined dielectric-metal stack of $\text{MgF}_2/\text{AlO}_x/\text{Ag}$. The processing scheme is shown in Figure 1b–f and detailed in Section 4. The dielectric-metal reflector leverages total internal reflection at the low refractive index dielectric for shallow angles, whereas for steeper angles still

specular reflection occurs at the subsequent metal layer.^[58,59] To realize low-ohmic semiconductor/metal contacts, for both reflector types the electrical rear contact is established via point contacts where locally the back reflector is opened and highly conductive point contacts are formed (about 1.8% areal coverage; Figure 1e).^[52,58,60,61] Under illumination, therefore, the generated current flows laterally toward these points. The top of Figure 1g shows an electroluminescence image of the PPC with Au reflector under forward bias, which reveals front and rear side features. The current flow in the device is illustrated by the lower three images in Figure 1g, which illustrate the voltage drop due to front grid and rear side point contacts in different layers of the device.

The absorber thickness of 1750 nm does not suffice to fully absorb photons with an energy close to the bandgap of the GaAs absorber ($E_g = 1.424 \text{ eV} \rightarrow \lambda = 871 \text{ nm}$) after single pass. Consequently, the SR of the reference device without reflector peaks at 830 nm (Figure 2a). In contrast, for the devices with back reflector a fringe pattern is observed in the SR close to the bandgap, resulting from Fabry–Perot resonances in the optical cavity. Peak $SR = 0.653 \text{ A W}^{-1}$ is obtained with the combined dielectric/metal reflector at $\lambda = 858 \text{ nm}$ (photon energy $hc/\lambda = 1.445 \text{ eV}$). Here, the related thermalization loss per photon reduces to 21 meV or 1%_{rel.} The corresponding external quantum efficiency (EQE) is $EQE(858 \text{ nm}) = (SR)hc/(q\lambda) = 94.4\%$. The spectral reflectance R reaches up to 93.7% and 95.5% for

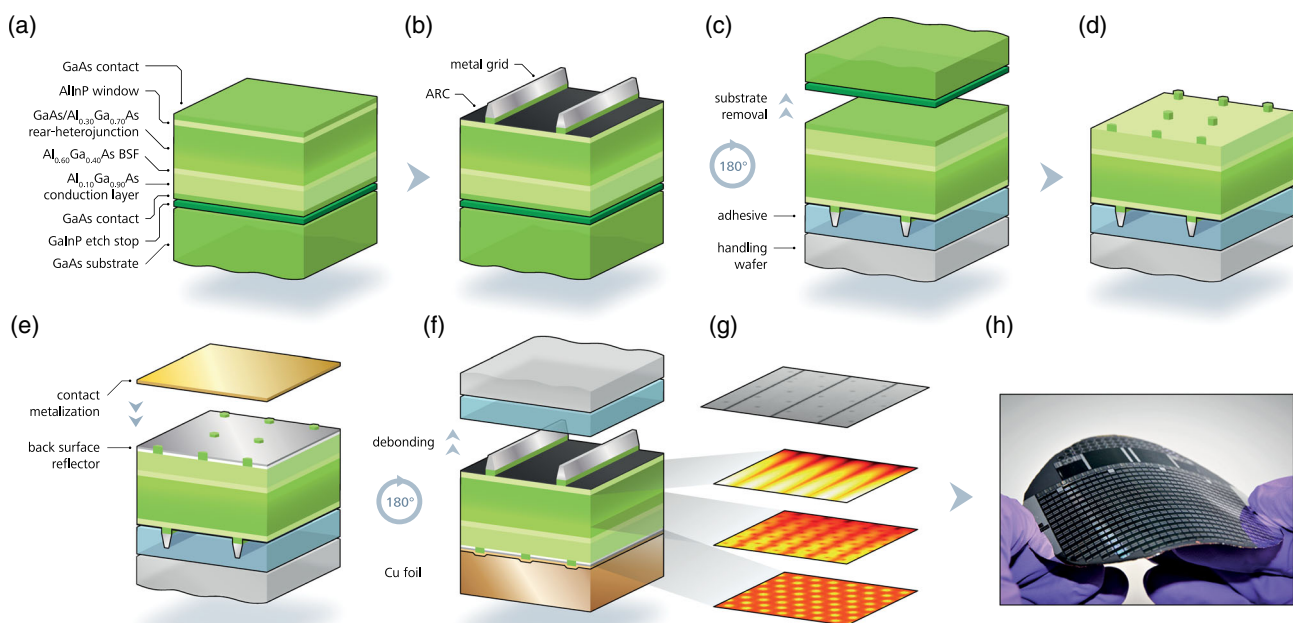


Figure 1. Illustration of the fabrication steps to realize the thin film PPCs with BSR in this work (see Section 4 for details). a) Epitaxial layer structure of the n-GaAs/p-AlGaAs rear-heterojunction device. b) Front side processing: grid metallization and antireflection coating (ARC). c) Transfer to handling wafer and substrate removal. d) Hexagonal point contact pattern on the rear side. e) Deposition of the structured BSR and rear side contact metallization. f) Cu electroplating to provide mechanical stabilization and debonding from handling wafer. g) Top: infrared microscopy image of a PPC with Au BSR and local point contacts under forward bias ($V = 1180 \text{ mV}$, $J_{\text{inj}} = 0.44 \text{ A cm}^{-2}$). The front metal grid lines prevent electroluminescence emission from underneath leading to dark line features in the image. The rear point contacts are visible as darker circles as there is no reflector underneath. Bottom: the lower three images illustrate the lateral voltage drop at the front and rear side due to metal front grid lines and rear point contacts, respectively, and at the junction influenced by both features. The images are obtained from electrical network modeling and show a different image section than the microscopy image above. h) Photography of a flexible 4'' wafer after thin film processing with BSR on copper foil.

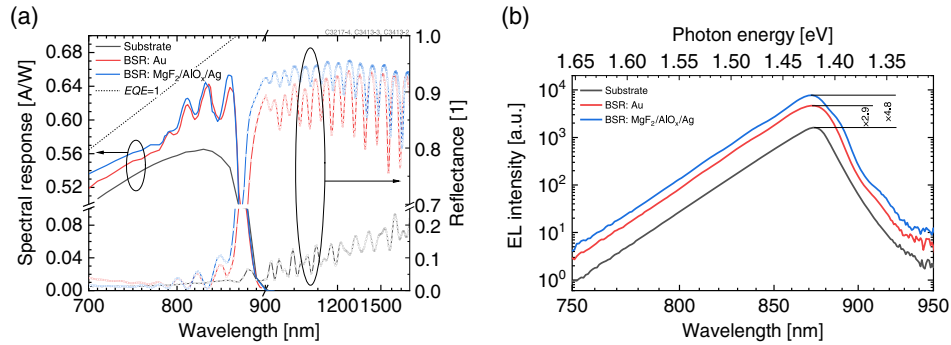


Figure 2. a) Calibrated SR at $T = 25^\circ\text{C}$ and SR R of the PPCs with BSR in comparison with a similar cell on substrate. b) Electroluminescence emission spectra of the cells under forward bias at an injection current density of $J_{\text{inj}} = 18.5\text{ A cm}^{-2}$.

PPCs with gold reflector and combined dielectric–silver reflector, respectively (cf., Figure 2a). The observed fringe pattern for sub-bandgap photons indicates the thin film interference. The back reflector also affects the device's electroluminescence emission (Figure 2b). With increasing reflectance of the back mirror, the electroluminescence intensity increases, namely, the peak intensity increases by a factor of 2.9 for the Au mirror and by

a factor of 4.8 for the dielectric–silver mirror compared with the reference on substrate.

Statistical analysis based on wafer-level I – V mapping under broad band flash light of hundreds of PPCs per wafer enables an assessment of how the back reflector changes the internal and external luminescence of the devices. The observed voltage gain (Figure 3a) corresponds with a drop in the median dark

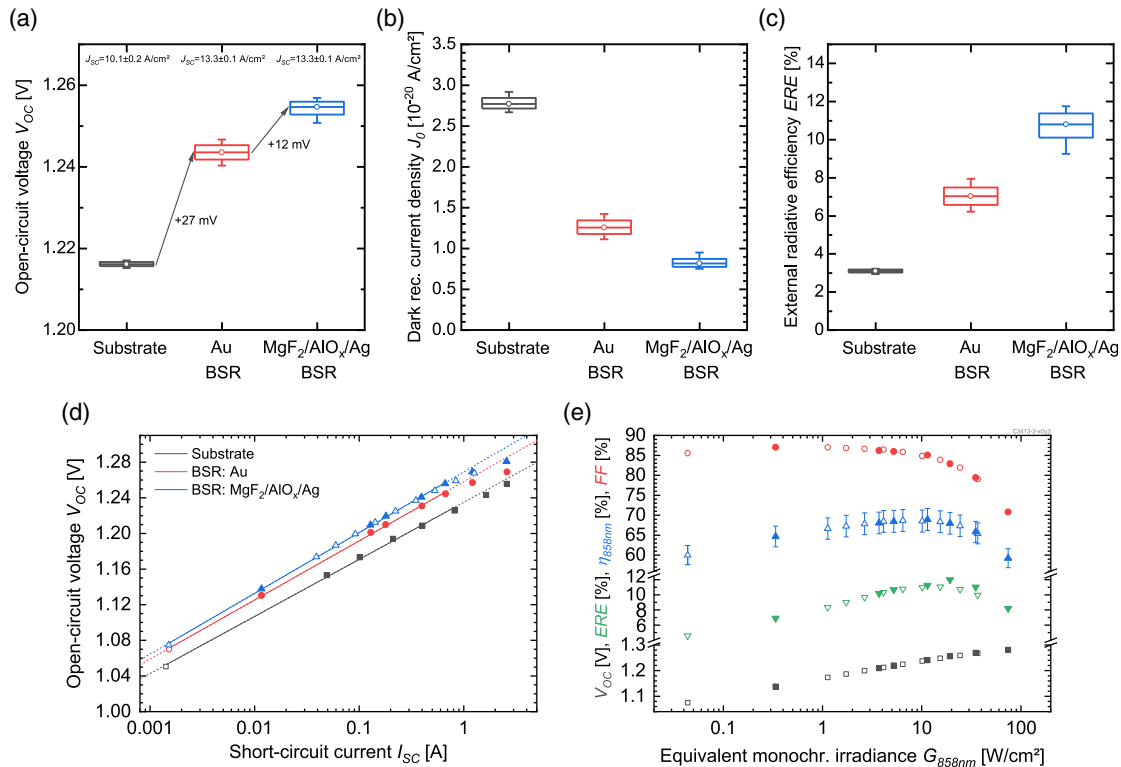


Figure 3. Box plots of a) open-circuit voltage (V_{OC}), b) dark recombination current density J_0 , and c) experimental ERE based on statistical data from wafer-level I – V mapping of PPCs on substrate and with BSRs, measured at short-circuit current densities of $J_{\text{SC}} = 10.1 \pm 0.2\text{ A cm}^{-2}$ (substrate) and $J_{\text{SC}} = 13.3 \pm 0.1\text{ A cm}^{-2}$ (BSR). The samples sizes are 468 (substrate), 381 (Au BSR), and 410 (MgF₂/AlO_x/Ag BSR). Boxes represent the first and third quartile with the median as central line. The mean value is plotted as a circle. Whiskers represent the 10th and 90th percentiles. d) V_{OC} as a function of short-circuit current (I_{SC}) for PPCs on substrate and with BSRs. e) V_{OC} , experimental ERE, equivalent monochromatic efficiency at 858 nm $\eta_{858\text{ nm}}$, and FF from light I – V measurements as a function of equivalent monochromatic irradiance at 858 nm $G_{858\text{ nm}}$. Open symbols in (d) and (e) represent measurements under broad band illumination, namely, under a calibrated 1 sun broad band light source (lowest current and irradiance, respectively) and using a Xenon flash bulb (rest). Solid symbols show data from I – V curves recorded under a pulsed 809 nm laser.^[66] Further details can be found in Section 4.

recombination current density J_0 from $2.8 \times 10^{-20} \text{ A cm}^{-2}$ for PPCs on substrate to $1.3 \times 10^{-20} \text{ A cm}^{-2}$ and $8.1 \times 10^{-21} \text{ A cm}^{-2}$ for gold and dielectric–silver reflectors, respectively. Assuming inverse proportion between J_0 and the carrier lifetime τ ,^[62] we conclude that photon recycling leads to a prolongation of the effective lifetimes in the n-type GaAs absorber by a factor of 2.2 and 3.4, respectively. Note that the dark recombination current density J_0 of the GaAs/AlGaAs rear-heterojunction on substrate is almost an order of magnitude lower than that of high-quality GaAs homojunction cells.^[39,63] In fact, fitting measured $I_{\text{SC}}-V_{\text{OC}}$ data to a one-diode model yields ideality factors n of 1.08, 1.12, and 1.15 for the PPC on substrate, with Au mirror, and with $\text{MgF}_2/\text{AlO}_x/\text{Ag}$ mirror, respectively (see Figure 3d). The proximity of the ideality factors to unity for the entire current range reveals that charge carrier recombination in the space charge region with $n = 2$ is negligible compared with the already low recombination in the n-type GaAs bulk. This can be explained with the absence of charge carrier generation in the base and Al grading region and the higher conduction band of AlGaAs. The latter results in a strong carrier selective field in the space charge region and, thus, further minimizes the concentration of electrons needed in the recombination process. The deviation from the expected logarithmic increase at high currents is attributed to heating which is more pronounced for the thin film wafers due to worse thermal coupling to the measurement chuck compared with the PPCs on stiff planar substrate and more pronounced for the broad band measurements due to the higher excess energy resulting in additional thermalization.

As to photon recycling, in an idealized cell the only remaining radiative recombination is light that can leave the system. Consequently, lowest recombination and thus highest voltage are achieved when external radiative efficiency (ERE), i.e., the percentage of recombination events that leads to an externally emitted photon, is maximal. Thus, the ERE is a figure of merit that not only describes the amount of radiative recombination inside the device, but also the overall radiative losses inside the optical system such as parasitic absorption in nonactive layers and imperfect reflection at the back reflector. As shown in Figure 3c, the median experimental ERE increases from 3.1% for the PPCs on substrate to 7.0% and 10.8% for PPCs with gold and dielectric–silver reflectors, respectively.

Finally, we determine the equivalent monochromatic efficiency η_λ using the calibrated $SR(\lambda)$ of the PPC (see Section 4). Figure 3e shows experimental data of V_{OC} , ERE , η_λ , and fill factor (FF) plotted against the equivalent monochromatic irradiance at peak SR , $G_{858 \text{ nm}} = P_{\text{in},858 \text{ nm}}/A$, for the champion PPC with $\text{MgF}_2/\text{AlO}_x/\text{Ag}$ reflector. Note that despite the different generation profiles in the absorber $I-V$ data measured under laser light (solid symbols) and under broad band spectrum (open symbols) are in very good agreement. With increasing irradiance, the efficiency increases as a result of the logarithmic increase in voltage until the peak efficiency of $\eta_{858 \text{ nm}} = 68.9 \pm 2.8\%$ is reached at $G_{858 \text{ nm}} = 11.4 \text{ W cm}^{-2}$. At higher irradiances, the performance is limited by ohmic losses, which results in a drop in FF and consequently in efficiency. Same as V_{OC} , ERE steadily increases with increasing irradiance until its rise is impaired by heating at irradiances above 20 W cm^{-2} and more pronounced under broad band light.

3. Conclusion

We have altered the boundary conditions for the tradeoff between thermalization and transmission losses for PPCs. By implementing a BSR to a thin film photovoltaic cell based on a high-quality GaAs/AlGaAs rear-heterojunction, we introduce an optical cavity to leverage optical resonance to increase near-bandgap absorptance as well as boost the output voltage due to photon recycling. Best performance is achieved with a $\text{MgF}_2/\text{AlO}_x/\text{Ag}$ reflector with which we have demonstrated an optical-to-electrical photovoltaic power conversion efficiency of $68.9 \pm 2.8\%$ for operation under monochromatic irradiance of 11.4 W cm^{-2} at 858 nm as determined using the equivalent monochromatic efficiency based on the calibrated SR . Highly efficient PPCs are a key ingredient to enable new and emerging applications of optical power transmission in various domains.

4. Methods

Epitaxial Growth: The n-GaAs/p-AlGaAs rear-heterojunction layer structure (see Figure 1a) is grown by metalorganic vapor-phase epitaxy (MOVPE) using an Aixtron AIX2800-G4-TM reactor with $8 \times 4''$ substrate configuration. The layer structure is grown on $4''$ p-type (100) GaAs substrates with 6° offcut toward $\langle 100 \rangle$ B and a nominal thickness of 450 μm . The epitaxial growth is based on the standard precursors arsine, phosphine, trimethylgallium, trimethylindium, and trimethylaluminum diluted in hydrogen carrier gas. Silane, dimethylzinc, and carbontetrabromide are used as doping sources. The pressure during growth is 50 mbar, process temperatures vary between 500 and 700 $^\circ\text{C}$, and V/III ratios between 2 and 35.

On the front side, the n-GaAs absorber (thickness $d = 1750$ and 2650 nm for the PPCs with BSR and on substrate, respectively, $n = 1 \times 10^{17} \text{ cm}^{-3}$) is passivated with a 25 nm n-AlInP window layer acting as a front surface field. A subsequent highly n-doped GaAs layer ($d = 400 \text{ nm}$, $n = 5 \times 10^{18} \text{ cm}^{-3}$) allows for low ohmic semiconductor/metal contact formation on the front side. The heterojunction is created by a gradual increase in the aluminum content below the n-type GaAs absorber to the p-type $\text{Al}_{0.30}\text{Ga}_{0.70}\text{As}$ base, which prevents from formation of hole barriers at the interfaces in the band diagram.^[57] The rear side is passivated with an $\text{Al}_{0.60}\text{Ga}_{0.40}\text{As}$ back surface field layer. Below the photovoltaic cell structure, a p- $\text{Al}_{0.10}\text{Ga}_{0.90}\text{As}$ layer ($d = 1400 \text{ nm}$, $p = 5 \times 10^{18} \text{ cm}^{-3}$) facilitates lateral majority carrier conduction towards the point contacts. Last, a highly doped p-GaAs layer ($d = 400 \text{ nm}$, $p = 1.4 \times 10^{19} \text{ cm}^{-3}$) enables low ohmic contact formation at the rear point contacts. A GaInP layer below this rear contact layer acts as an etch stop layer during the wet chemical substrate removal process.

Device Fabrication: After epitaxial growth, the thin-film processing of the wafers is conducted based on the following processing chain. First, the front side is processed, including structured wet etching of the front n-GaAs contact layer between the grid fingers and subsequent evaporation and lift-off of a Pd/Au/Ge/Ti/Pd/Ag front contact metallization with a total thickness of 3200 nm. The front grid features a comb structure with parallel fingers with a pitch of 146 μm . The grid fingers end on both sides in 250 μm wide busbars. The contacts are annealed for 1 min at 290 $^\circ\text{C}$. The specific contact resistivity determined with transmission line measurements is in the range $r_c = 1-4 \times 10^{-6} \Omega \text{ cm}^2$. In a selective mesa etching step, trenches into the layer structure are etched between individual cells until the p- $\text{Al}_{0.60}\text{Ga}_{0.40}\text{As}$ back surface field layer is exposed. Phosphides are etched using hydrochloride, and arsenides are etched with a citric acid: hydrogen peroxide = 3:1 solution. Individual chip dimensions are nominally $2.23 \times 2.87 \text{ mm}^2$. The nominal designated area is $A = 0.054 \text{ cm}^2$. The actual designated area, as measured by optical microscopy, deviates by about 1–3% from the nominal value due to lateral etch variations in the mesa etching process. At last, the front side is coated with a

ZnS/YF₃ = 52/80 nm two-layer antireflection coating (ARC) (Ta₂O₅/MgF₂ = 52/80 nm for the PPCs on substrate), which is lifted from the bus-bars to allow for electrical contact (Figure 1b). Once the front side processing is completed, the wafer is temporarily bonded to a 4" sapphire wafer. Then, the GaAs substrate is wet chemically removed with a hydrogen peroxide:33% aqueous ammonia = 5:1 solution. After substrate removal, the GaInP etch stop layer is removed by dipping in hydrochloride (Figure 1c). To realize the structured BSR first, a photolithography is conducted to locally protect the small point areas (hexagonal pattern, 10 μm diameter, 100 μm pitch). Then, the rear p-GaAs contact layer is etched and subsequently either Au is evaporated or MgF₂ is evaporated followed by sputter deposition of AlO_x and subsequently Ag. The rear side contact points are then opened again by stripping the resist and lift-off. Finally, a Pd/Zn/Pd/Au rear side metal contact is evaporated, i.e., on the reflector as well as the exposed point contacts (Figure 1e). Last, a flexible 30 μm-thick Cu foil is electroplated on the rear to provide mechanical stabilization. Afterward the now completed thin film structure is debonded from the sapphire handling wafer (Figure 1f).

Device Characterization: All measurements are conducted on wafer level, i.e., no cell singulation is performed. Relative SR (SR_{rel}) and relative EQE (EQE_{rel}) = (SR_{rel})/($hc/(q\lambda)$) are measured using a grating monochromator setup^[64] with adjustable bias voltage and bias spectrum on a temperature-controlled chuck ($T = 25^\circ\text{C}$). For most of the wavelength range, the measurement is conducted in 10 nm steps (standard configuration). To increase the accuracy in vicinity of the bandgap, in the range 780–890 nm the resolution is increased by decreasing the entrance and exit slit widths of the grating monochromator (monochromatic light with 3 nm full width at half maximum (FWHM)) and the measurement is conducted in 2 nm steps. The actual designated area A is determined using an optical microscope. One-sun I - V characteristics are measured on a temperature-controlled chuck ($T = 25^\circ\text{C}$) under a spectrally adjustable sun simulator to generate the same short-circuit current as under illumination with the AM1.5d (ASTM G173-03) spectrum $E(\lambda)$ ($\int E d\lambda = 1000 \text{ W m}^{-2}$). The spectral irradiance of the sun simulator is determined with a spectroradiometer which is calibrated using a standard lamp. The intensity of the sun simulator is determined with a reference solar cell. Both standard lamp and reference solar cell are calibrated at the Physikalisch-Technische Bundesanstalt, the National Metrology Institute of Germany, traceable to national standards and, thus, to the international system of units (SI). The calibrated absolute SR is then determined as follows

$$SR = \frac{I_{SC}/A}{\int SR_{rel} E d\lambda} SR_{rel} \quad (1)$$

Wafer-level I - V mapping is conducted on a temperature-controlled chuck ($T = 25^\circ\text{C}$) using a broad band flash light (Xenon flash bulb) based setup. The I - V curve is recorded within 600 μs at the peak of the irradiance. The remaining irradiance variation during the measurement is corrected for using a monitor cell. It is remarked that the I - V mapping of the PPCs on substrate has been conducted at slightly lower currents ($I_{SC} = 548 \pm 12 \text{ mA}$) than the PPCs with back reflector ($I_{SC} = 718 \pm 6 \text{ mA}$). This current difference accounts for 8 mV of the difference in V_{OC} in Figure 3a. In addition to the I - V mapping, the irradiance-dependent I - V characteristics of the champion cell are measured under a different broad band flash light based setup (Xenon flash bulb, voltage sweep time 1 ms, temperature-controlled chuck $T = 25^\circ\text{C}$) and the irradiance is varied by changing the distance between flash bulb and device under test.^[65] In this case, possible hysteresis effects are ruled out by comparison of the I - V curves measured in forward (from I_{SC} to V_{OC}) and backward (from V_{OC} to I_{SC}) direction. I - V parameters are determined from the average of the two measurements. Further light I - V measurements of individual cells are conducted using a laser-based transient measurement setup with temperature-controlled chuck ($T = 25^\circ\text{C}$).^[66] Here, similar to broad band flash light measurements, I - V curves are recorded within 1 ms during pulsed laser illumination (DILAS Compact-Mini 50 W; $\lambda = 809 \text{ nm}$, 3 nm full width at half maximum, homogenized

beam spot larger than the device under test), and I - V parameters are determined from the average of forward and backward measurements.

For light I - V measurements, we can derive the corresponding equivalent monochromatic input power $P_{in,\lambda} = I_{SC}/SR(\lambda)$. With P_{mp} being the measured maximum output power, the equivalent monochromatic efficiency η_λ is determined from measured quantities as follows

$$\eta_\lambda = \frac{P_{mp}}{P_{in,\lambda}} = \frac{P_{mp} SR(\lambda)}{I_{SC}} \quad (2)$$

This η_λ is the efficiency of the PPC under monochromatic illumination of wavelength λ ,^[67] sometimes also called spectral efficiency and expressed by the derived quantity $FF: \eta_\lambda = (SR)(V_{OC})(FF)$.^[68,69] Note that this equivalent efficiency approach is only valid for devices where the device response is linear with irradiance and where the EQE does not depend on the minority carrier generation profile in the absorber, which holds for decent passivated materials with sufficient diffusion lengths. The agreement of the data in Figure 3e obtained from measurements under different illumination spectra (809 nm laser light and broad band xenon lamp emission) validates this assumption. It is emphasized that the aforementioned assumptions typically do not hold, e.g., for lower quality devices and neither for multijunction devices. For the latter, the device current strongly depends on the generation profile due to the series connection of subcells; and in addition, luminescence coupling between the junctions often leads to nonlinear behavior.

For the champion cell results shown in Figure 3e, an error propagation analysis is conducted on Equation (2). The plotted error bars represent uncertainties in the determination of P_{mp} , I_{SC} , and SR .

The electroluminescence spectrum of the PPCs under forward bias is measured using a fiber coupled spectrometer (Tec5 PDA). The data of two Si-based CCD line sensors for the spectral ranges 300–720 nm and 695–1100 nm are merged by data processing after the measurement. The fiber tips (600 μm) are positioned at the same distance above the device; a stepper motor is used to place them at the same position. The measurements have been performed with equal position and settings, but without further calibration. Thus, the data are to be considered valid only in relative terms. Electroluminescence imaging is performed using a silicon CCD camera (Andor Luca EMCCD A-DL604M) positioned above the device under test, while a current source injects current in forward bias to operate the device in LED mode.

Derivation of J_0 and ERE from I - V Data: From the one-diode model, we can derive the dark recombination current density J_0

$$J_0 = \frac{I_{SC}}{A [\exp(\frac{qV_{OC}}{nkT}) - 1]} \quad (3)$$

with electron charge q , Boltzmann's constant k , and temperature $T = 298.15 \text{ K}$. To enable valid comparison of J_0 data of different devices, for the determination of J_0 data in Figure 3b an equal ideality factor of $n = 1$ is assumed.

According to Rau's reciprocity theorem^[70] the ERE, i.e., the percentage of recombination events that leads to an externally emitted photon, can be deduced from I_{SC} , V_{OC} , and the EQE^[71,72]

$$ERE = \frac{J_0^{rad}}{J_0} = \frac{A}{I_{SC}} \frac{2\pi q}{h^3 c^2} \exp\left(\frac{qV_{OC}}{kT}\right) \int \frac{EQE^2}{\exp(\frac{E}{kT}) - 1} dE \quad (4)$$

with J_0^{rad} being the radiative recombination current density, h Planck's constant, c the speed of light, and EQE the angular weighted EQE, which for high-quality cells can be approximated with the near-perpendicular EQE.^[71]

Acknowledgements

The authors gratefully thank Fraunhofer ISE coworkers D. Chojniak, E. Fehrenbacher, A. Franke, R. Freitas, S. Heckelmann, J. Köhler, C. Kopiniok, J. Markert, F. Martin, M. Mundus, G. Mikolasch, E. Oliva,

E. Paz Alpuche, S.K. Reichmuth, L.A. Ruiz Preciado, E. Schäffer, P. Schygulla, G. Siefer, S. Stättner, and A. Wekkeli for support with epitaxial growth, semiconductor processing, device characterization as well as for many valuable discussions. Also, the authors thank O. Göhlich from Fraunhofer IAF for ZnS/YF₃ deposition. The work was partly funded by the German Federal Ministry of Education and Research (BMBF) through the project "Lightbridge" (grant no. 16ES0788). E.L. acknowledges an Atracción del Talento Fellowship (2019-T2/AMB-12959) funded by the Comunidad de Madrid.

Open access funding enabled and organized by Projekt DEAL.

Conflict of Interest

The authors declare no conflict of interest.

Data Availability Statement

Research data are not shared.

Keywords

back reflectors, optical power transmission, photon recycling, photonic power converters, resonance

Received: February 25, 2021

Revised: March 11, 2021

Published online: May 4, 2021

- [1] H. Helmers, D. Lackner, G. Siefer, E. Oliva, F. Dimroth, A. W. Bett, in *Proc. 32nd European Photovoltaic Solar Energy Conf. and Exhibition*, WIP, Munich, Germany **2016**, p. 218.
- [2] D. Kamiyama, A. Yoneyama, M. Matsuura, *IEEE Photon. Technol. Lett.* **2018**, *30*, 646.
- [3] A. Ahnood, J. P. Ndobakuranye, S. Li, O. Kavehei, S. Praver, *Eng. Res. Express* **2020**, *2*, 15036.
- [4] J. Fakidis, H. Helmers, H. Haas, *IEEE Photonics Technol. Lett.* **2020**, *32*, 1277.
- [5] H. Helmers, C. Armbruster, M. von Ravenstein, D. Derix, C. Schoner, *IEEE Trans. Power Electron.* **2020**, *35*, 7904.
- [6] K. Worms, C. Klamouris, F. Wegh, L. Meder, D. Volkmer, S. P. Philipps, S. K. Reichmuth, H. Helmers, A. Kunadt, J. Vourvoulakis, A. W. Bett, C. Koos, W. Freude, J. Leuthold, W. Stork, *Wind Energy* **2017**, *20*, 345.
- [7] A. Andersson, D. Destefan, J. D. Ramboz, S. Weiss, J. M. DeHaan, in *2001 IEEE/PES Transmission and Distribution Conf. and Exposition. Developing New Perspectives (Cat. No.01CH37294)*, IEEE, Piscataway, NJ, USA **2001**, pp. 379–384, <https://doi.org/10.1109/TDC.2001.971264>.
- [8] F. V. B. de Nazare, M. M. Werneck, *IEEE Sensors J.* **2012**, *12*, 1193.
- [9] J. B. Rosolem, F. R. Bassan, R. S. Penze, C. Florida, A. A. Leonardi, F. R. Pereira, C. A. M. Nascimento, *IEEE Trans. Power Delivery* **2015**, *30*, 1449.
- [10] P. Wei, S. Lu, H. Huang, L. Deng, J. Zhao, *Proc. SPIE*, **2018**, *10812*, 108121A.
- [11] K. Goto, T. Nakagawa, O. Nakamura, S. Kawata, *IEEE Trans. Biomed. Eng.* **2001**, *48*, 830.
- [12] C. Algara, R. Peña, *Artif. Organs* **2009**, *33*, 855.
- [13] M. Mujeeb-U-Rahman, D. Adalian, C.-F. Chang, A. Scherer, *J. Biomed. Opt.* **2015**, *20*, 95012.
- [14] E. Moon, D. Blaauw, J. D. Phillips, *IEEE Trans. Electron Devices* **2017**, *64*, 2432.
- [15] A. Ahnood, R. Cheriton, A. Bruneau, J. A. Belcourt, J. P. Ndobakuranye, W. Lemaire, R. Hilkes, R. Fontaine, J. P. D. Cook, K. Hinzer, S. Praver, *Adv. Biosyst.* **2020**, *4*, e2000055.
- [16] X. Zhang, H. Li, J. A. Brothers, L. Fu, M. Perales, J. Wu, J. Wang, *IEEE J. Emerg. Sel. Topics Power Electron.* **2016**, *4*, 946.
- [17] P. Wei, C. Zhao, H. Huang, S. Lu, C. Li, H. Deng, *Opt. Eng.* **2019**, *58*, 1.
- [18] M. M. Wilkins, M. Ishigaki, P.-O. Provost, D. Masson, S. Fafard, C. E. Valdivia, E. M. Dede, K. Hinzer, *IEEE Trans. Power Electron.* **2019**, *34*, 1054.
- [19] T. Umezawa, P. T. Dat, K. Kashima, A. Kanno, N. Yamamoto, T. Kawanishi, *J. Lightwave Technol.* **2018**, *36*, 617.
- [20] C. Vazquez, J. D. Lopez-Cardona, P. C. Lallana, D. S. Montero, F. M. A. Al-Zubaidi, S. Perez-Prieto, I. Perez Garcilopez, *IEEE Access* **2019**, *7*, 158409.
- [21] M. Matsuura, H. Nomoto, H. Mamiya, T. Higuchi, D. Masson, S. Fafard, *IEEE Trans. Power Electron.* **2021**, *36*, 4532.
- [22] H. Miyakawa, Y. Tanaka, T. Kurokawa, *Appl. Opt.* **2004**, *43*, 1379.
- [23] M. Röger, W. Freude, G. Böttger, M. Dreschmann, M. Huebner, C. Klamouris, A. W. Bett, J. Becker, J. Leuthold, *Opt. Express* **2008**, *16*, 21821.
- [24] P. D. Diamantoulakis, G. K. Karagiannidis, Z. Ding, *IEEE Trans. Green Commun. Netw.* **2018**, *2*, 764.
- [25] Q. Liu, J. Wu, P. Xia, S. Zhao, W. Chen, Y. Yang, L. Hanzo, *IEEE Veh. Technol. Mag.* **2016**, *11*, 36.
- [26] K. Jin, W. Zhou, *IEEE Trans. Power Electron.* **2018**, 3842.
- [27] Q. Zhang, W. Fang, Q. Liu, J. Wu, P. Xia, L. Yang, *IEEE Internet Things J.* **2018**, *1*.
- [28] J. Lim, T. S. Khwaja, J. Ha, *Opt. Express* **2019**, *27*, A924.
- [29] P. Jaffe, in *Future Energy: Improved, Sustainable and Clean Options for Our Planet* (Ed.: T. M. Letcher), Elsevier, Amsterdam, The Netherlands **2020**, p. 519.
- [30] L. C. Olsen, D. A. Huber, G. Dunham, F. W. Addis, in *Conf. Record of the Twenty-Second IEEE Photovoltaic Specialists Conf. - 1991*, Vol. 1, IEEE, Piscataway, NJ, USA **1991**, pp. 419–424, <https://doi.org/10.1109/PVSC.1991.169250>.
- [31] D. Krut, R. Sudharsanan, T. Isshiki, R. King, N. H. Karam, in *2007 65th Annual Device Research Conf.*, IEEE, Piscataway, NJ, USA **2007**, pp. 123–124, <https://doi.org/10.1109/DRC.2007.4373680>.
- [32] E. Oliva, F. Dimroth, A. W. Bett, *Prog. Photovoltaics* **2008**, *4*, 289.
- [33] J. Schubert, E. Oliva, F. Dimroth, W. Guter, R. Löckenhoff, A. W. Bett, *IEEE Trans. Electron Devices* **2009**, *56*, 170.
- [34] J. Mukherjee, S. Jarvis, M. Perren, S. J. Sweeney, *J. Phys. D: Appl. Phys.* **2013**, *46*, 264006.
- [35] H. Helmers, L. Wagner, C. Garza, S. Reichmuth, E. Oliva, S. P. Philipps, D. Lackner, A. W. Bett, in *Proc. SENSOR 2015, AMA, Wunstorf, Germany 2015*, p. 519, <https://doi.org/10.5162/sensor2015/D1.4>.
- [36] M. M. Wilkins, C. E. Valdivia, A. M. Gabr, D. Masson, S. Fafard, K. Hinzer, *J. Appl. Phys.* **2015**, *118*, 143102.
- [37] S. Fafard, F. Proulx, M. C. A. York, L. S. Richard, P. O. Provost, R. Arès, V. Aimez, D. P. Masson, *Appl. Phys. Lett.* **2016**, *109*, 131107.
- [38] S. Fafard, M. C. A. York, F. Proulx, C. E. Valdivia, M. M. Wilkins, R. Arès, V. Aimez, K. Hinzer, D. P. Masson, *Appl. Phys. Lett.* **2016**, *108*, 71101.
- [39] O. Höhn, A. W. Walker, A. W. Bett, H. Helmers, *Appl. Phys. Lett.* **2016**, *108*, 241104.
- [40] Y. Zhao, Y. Sun, Y. He, S. Yu, J. Dong, *Sci. Rep.* **2016**, *6*, 38044.
- [41] F. Proulx, M. C. A. York, P. O. Provost, R. Arès, V. Aimez, D. P. Masson, S. Fafard, *Phys. Status Solidi RRL* **2017**, *11*, 1600385.

- [42] S. K. Reichmuth, H. Helmers, S. P. Philipps, M. Schachtner, G. Siefer, A. W. Bett, *Prog. Photovoltaics* **2017**, 25, 67.
- [43] J. Huang, Y. Sun, Y. Zhao, S. Yu, K. Li, J. Dong, J. Xue, C. Xue, Y. Ye, *J. Semicond.* **2018**, 39, 94006.
- [44] V. P. Khvostikov, S. V. Sorokina, N. S. Potapovich, O. A. Khvostikova, N. K. Timoshina, M. Z. Shvarts, *Semiconductors* **2018**, 52, 366.
- [45] G. Keller, D. Fuhrmann, T. Wierzkowski, A.-K. Volk, B. Fuhrmann, L. Horst, C. Wächter, M. Schauerte, H. Helmers, V. Khorenko, in *Tech. Dig. of the 1st Optical Wireless and Fiber Power Transmission Conf. (OWPT2019)*, **2019**, p. 11.
- [46] R. Kimovec, H. Helmers, A. W. Bett, M. Topič, *Prog. Photovoltaics* **2019**, 27, 199.
- [47] Y. Zhao, P. Liang, H. Ren, P. Han, *AIP Adv.* **2019**, 9, 105206.
- [48] H. Helmers, A. Franke, D. Lackner, O. Höhn, F. Predan, F. Dimroth, in *2020 47th IEEE Photovoltaic Specialists Conf. (PVSC)*, IEEE, Piscataway, NJ, USA **2020**, pp. 2471–2474, <https://doi.org/10.1109/PVSC45281.2020.9300717>.
- [49] N. A. Kalyuzhnyy, V. M. Emelyanov, V. V. Evstropov, S. A. Mintairov, M. A. Mintairov, M. V. Nahimovich, R. A. Salii, M. Z. Shvarts, *Sol. Energy Mater. Sol. Cells* **2020**, 217, 110710.
- [50] E. Lopez, O. Höhn, M. Schauerte, D. Lackner, M. Schachtner, S. K. Reichmuth, H. Helmers, *Prog. Photovoltaics* **2021**, 29, 461.
- [51] H.-L. Chen, A. Cattoni, R. D. Lépinau, A. W. Walker, O. Höhn, D. Lackner, G. Siefer, M. Faustini, N. Vandamme, J. Goffard, B. Behaghel, C. Dupuis, N. Bardou, F. Dimroth, S. Collin, *Nat. Energy* **2019**, 4, 761.
- [52] I. Massiot, A. Cattoni, S. Collin, *Nat. Energy* **2020**, 5, 959.
- [53] G. Lush, M. Lundstrom, *Sol. Cells* **1991**, 30, 337.
- [54] O. D. Miller, E. Yablonovitch, S. R. Kurtz, *IEEE J. Photovolt.* **2012**, 2, 303.
- [55] U. Rau, U. W. Paetzold, T. Kirchartz, *Phys. Rev. B Condens. Matter* **2014**, 90.
- [56] Y. Takeda, *Appl. Phys. Express* **2020**, 13, 54001.
- [57] S.-T. Hwang, S. Kim, H. Cheun, H. Lee, B. Lee, T. Hwang, S. Lee, W. Yoon, H.-M. Lee, B. Park, *Sol. Energy Mater. Sol. Cells* **2016**, 155, 264.
- [58] C. L. Schilling, O. Höhn, D. N. Micha, S. Heckelmann, V. Klinger, E. Oliva, S. W. Glunz, F. Dimroth, *IEEE J. Photovolt.* **2018**, 8, 348.
- [59] D. N. Micha, O. Höhn, E. Oliva, V. Klinger, A. W. Bett, F. Dimroth, *Prog. Photovoltaics* **2019**, 27, 163.
- [60] N. Gruginskie, S. van Laar, G. Bauhuis, P. Mulder, M. van Eerden, E. Vlieg, J. J. Schermer, *Thin Solid Films* **2018**, 660, 10.
- [61] S.-T. Hwang, T. Hwang, S. Lee, B. Gil, B. Park, *Sol. Energy Mater. Sol. Cells* **2018**, 182, 348.
- [62] S. M. Sze, *Physics of Semiconductor Devices*, Wiley, New York **1981**.
- [63] M. Steiner, S. P. Philipps, M. Hermle, A. W. Bett, F. Dimroth, *Prog. Photovoltaics* **2010**, 19, 73.
- [64] G. Siefer, T. Gandy, M. Schachtner, A. Wekkeli, A. W. Bett, in *2013 IEEE 39th Photovoltaic Specialists Conf. (PVSC)*, IEEE, Piscataway, NJ, USA **2013**, pp. 86–89, <https://doi.org/10.1109/PVSC.2013.6744105>.
- [65] G. Siefer, P. Abbott, C. Baur, T. Schlegel, A. W. Bett, in *Proc. 20th European Photovoltaic Solar Energy Conf.*, WIP, Munich, Germany **2005**, p. 495.
- [66] S. K. Reichmuth, H. Helmers, C. E. Garza, D. Vahle, M. de Boer, L. Stevens, M. Mundus, A. W. Bett, G. Siefer, in *Proc. 32nd European Photovoltaic Solar Energy Conf. and Exhibition*, WIP, Munich, Germany **2016**, p. 5; <https://doi.org/10.4229/EUPVSEC20162016-1AO.1.2>.
- [67] A. W. Bett, F. Dimroth, R. Löckenhoff, E. Oliva, J. Schubert, in *2008 33rd IEEE Photovoltaic Specialists Conf.*, IEEE, Piscataway, NJ, USA **2008**, <https://doi.org/10.1109/PVSC.2008.4922910>.
- [68] M. A. Hamdy, F. Luttmann, D. Osborn, *Appl. Energy* **1988**, 30, 209.
- [69] Z. Yu, M. Leilaieoun, Z. Holman, *Nat. Energy* **2016**, 1, 16137.
- [70] U. Rau, *Phys. Rev. B Condens. Matter* **2007**, 76, 085303-1.
- [71] M. A. Green, *Prog. Photovoltaics* **2012**, 20, 472.
- [72] T. Kirchartz, U. Rau, *Adv. Energy Mater.* **2018**, 8, 1703385.